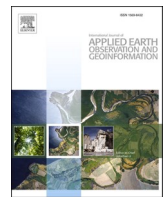


Contents lists available at ScienceDirect

# International Journal of Applied Earth Observations and Geoinformation

journal homepage: [www.elsevier.com/locate/jag](http://www.elsevier.com/locate/jag)



## Precursory motion and deformation mechanism of the 2018 Xe Pian-Xe Namnoy dam Collapse, Laos: Insights from satellite radar interferometry

Lei Xie<sup>a</sup>, Wenbin Xu<sup>b,\*</sup>, Xiaoli Ding<sup>a</sup>

<sup>a</sup> The Department of Land Surveying and Geo-Informatics, The Hong Kong Polytechnic University, China

<sup>b</sup> Laboratory of Volcano and Earthquake Research, School of Geosciences and Info-physics, Central South University, China

### ARTICLE INFO

#### Keywords:

Dam failure  
Hydrological hazard  
InSAR  
Xe Pian-Xe Namnoy project  
Independent component analysis  
Deformation mechanism

### ABSTRACT

The sudden failure of hydraulic dams poses catastrophic hydrological risks to local communities and environments. The 2018 Xe Pian-Xe Namnoy Dam collapse in Southern Laos unleashed a flood wall that resulted in more than 70 deaths and left thousands homeless. While the causes of this event were clearly known as geological and engineering issues, the detailed process of dam degradation and potential hazards of other dams in the area remain unclear. In this study, we use radar satellites to investigate the precursory deformation of major dams in the Xe Pian-Xe Namnoy hydropower project. By combining independent component analysis and an Earth loading model to decompose the observed deformation into various time-dependent components, we study the possible deformation mechanism. We identify a precursory vertical deformation acceleration on the collapsed Saddle Dam D reaching up to 13 cm/yr two months before the failure. Two earth-fill saddle dams (E and F) also experienced accelerating subsidence of ~9 cm/yr two months before the dam failure. The deformation pattern of these saddle dams resembles that of the collapsed Saddle Dam D, indicating a critical need for reinforcement interventions before being returned to service. In comparison, the rock-fill Xe Pian and Xe Namnoy Dams were relatively stable before the 2018 failure event. We show that water pressure, consolidation, thermal expansion, and precursory acceleration are the major mechanisms controlling dam deformation. Our results provide additional details for understanding the cause of the dam-break, and also to warn that other saddle dams associated with the project may also break if no further treatment is done. In addition, this study demonstrates the importance of space-borne radar interferometry and hybrid data analysis for early warning and hydrological safety management of small-to-medium-size dams, where *in situ* monitoring systems are often unavailable.

### 1. Introduction

Hydropower dams utilize the potential and kinetic energy of water. Globally, in the 2010s, more than 3,700 dams were either planned or under construction (Moran et al., 2018). With this boom in hydro-dam development, dam safety has become a major concern (Li et al., 2020). According to a 2011 International Commission on Large Dams (ICOLD) report, over 90% of dam failures have occurred on small dams (Pisaniello et al., 2015). In recent five years, most water-retaining dam collapse events involve small-to-medium sized dams with heights of  $\leq 30$  m (Table S1). In addition, there still exist a number of small-to-medium-sized hydraulic dams that cannot be effectively monitored using instrumental techniques (Lempérière, 2017).

Owing to its characteristics of low labor requirements, high spatial resolution, and affordability, interferometric synthetic aperture radar

(InSAR) has been introduced for dam safety monitoring applications (Scaioni et al., 2018). However, most effort has been placed in demonstrating the capability of InSAR in monitoring concrete arch dams and high gravity dams (typically at least 100 m in height), such as the Perthusillo Dam (Italy), the Three Gorges Dam (China), the Baixo Sabor Dam (Portugal), and the Aswan Dam (Egypt) (Milillo et al., 2016; Roque et al., 2021; Wang et al., 2011). Although validating the use of InSAR for the structural safety assessment of these large dams is important, these high-profile dams are generally well monitored by multiple on-site systems (e.g., inclinometers and laser ranging) (Scaioni et al., 2018). In contrast, very few studies have documented dam deformation patterns in small-to-medium-sized dams (embankments) and hydro-dam failure events (Cheng et al., 2019).

To improve understanding of deformation of small-to-medium-sized dams and to mitigate the risk of future catastrophic events, we study the

\* Corresponding author.

E-mail address: [wenbin.xu@csu.edu.cn](mailto:wenbin.xu@csu.edu.cn) (W. Xu).

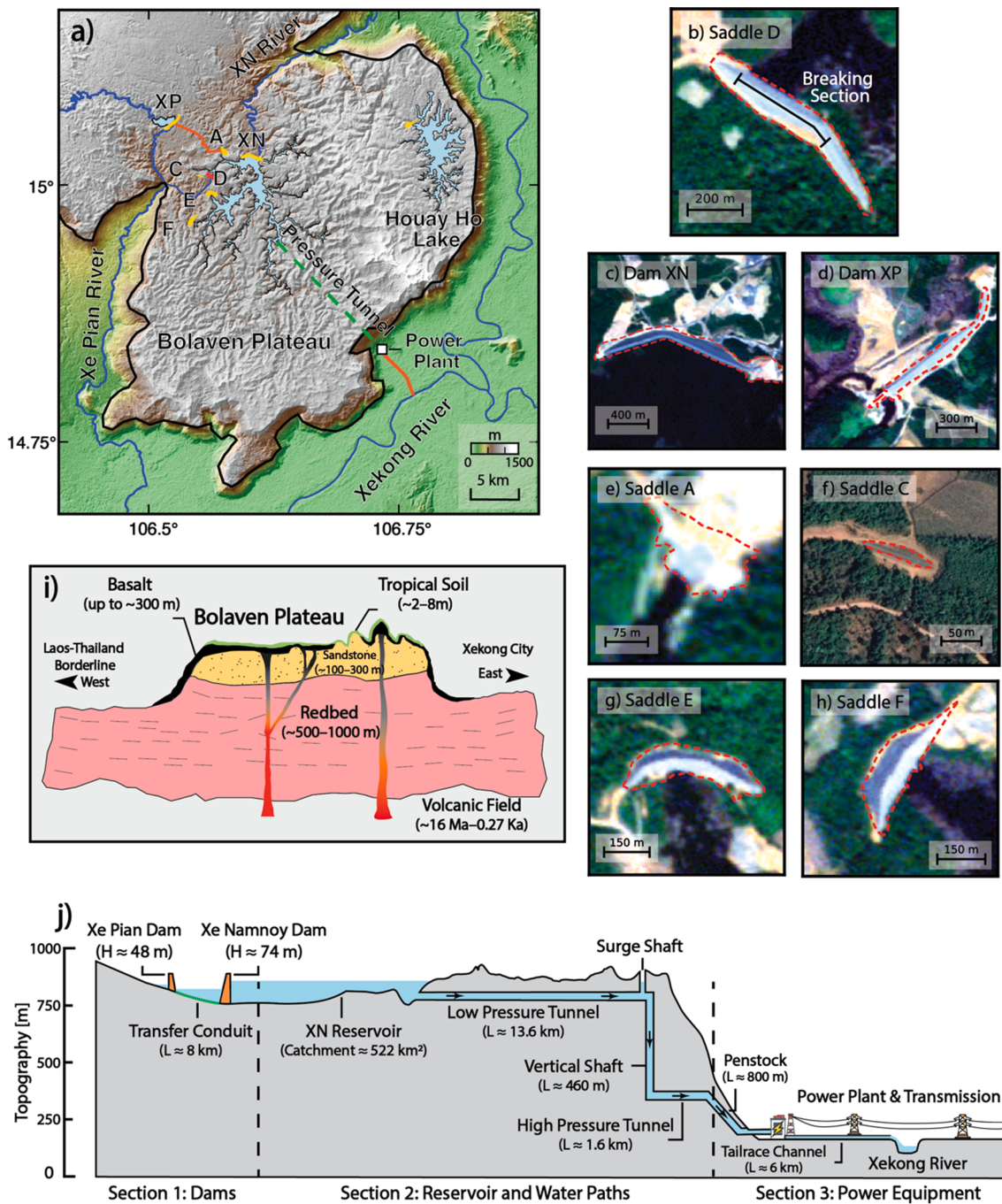


**Fig. 1.** The maps of the XPXN project. a) The geographic map of the XPXN project (orange lines denote the channel and conduits). b)–h) The enlarged landscape of two rock-fill dams and five saddle dams (The basemaps are from the RapidEye-3 and Google Earth). i) A simplified N-E geological profile across the Bolaven Plateau (from Laos-Thailand border to Xekong city, Latrubblesse et al., 2020). j) The ~ 40-km length cross-section of the XPXN project (from Xe-Pian Xe-Namnoy Power Co., Ltd.). (For interpretation of the references to color in this figure legend, the reader is referred to the web version of this article.)

2018 Xe Pian-Xe Namnoy (XPXN) collapse event in Laos from a space-borne perspective. We present detailed motion patterns of a cluster of dams (i.e., the collapsed Saddle Dam D and an additional four intact dams that are part of the same overall project) based on multi-geometry InSAR data. We adopt a hybrid approach combining independent component analysis (ICA) and the layered Earth loading model to decompose the observed deformation into time-dependent components, enabling the detailed study of the physical processes on the collapsed Saddle Dam D. We show that these methods can be used to identify potential risks as well as shed light on the underpinning deformation mechanisms in small-to-medium-sized dams.

## 2. Study area

The XPXN hydropower project lies on the Bolaven Plateau, a basaltic volcanic plateau that was abruptly uplifted ~ 1 km from the Xekong River (Fig. 1a and Fig. 1i; Latrubblesse et al., 2020). The topmost volcanic basalt has been weathered to form 2–8 m tropical soils with silty and sandy layers (Sanematsu et al., 2011). The outcrops of basaltic volcanic rocks near the reservoir are alkaline basalt (~ 16 Ma) and tholeiitic basalt (~ 1 Ma), which lie on the ~ 100–300-m-deep flat-flying bedrock. These horizontal bedrock structure suggests that the Bolaven Plateau is generally not tectonically active, with very few mapped fault lines

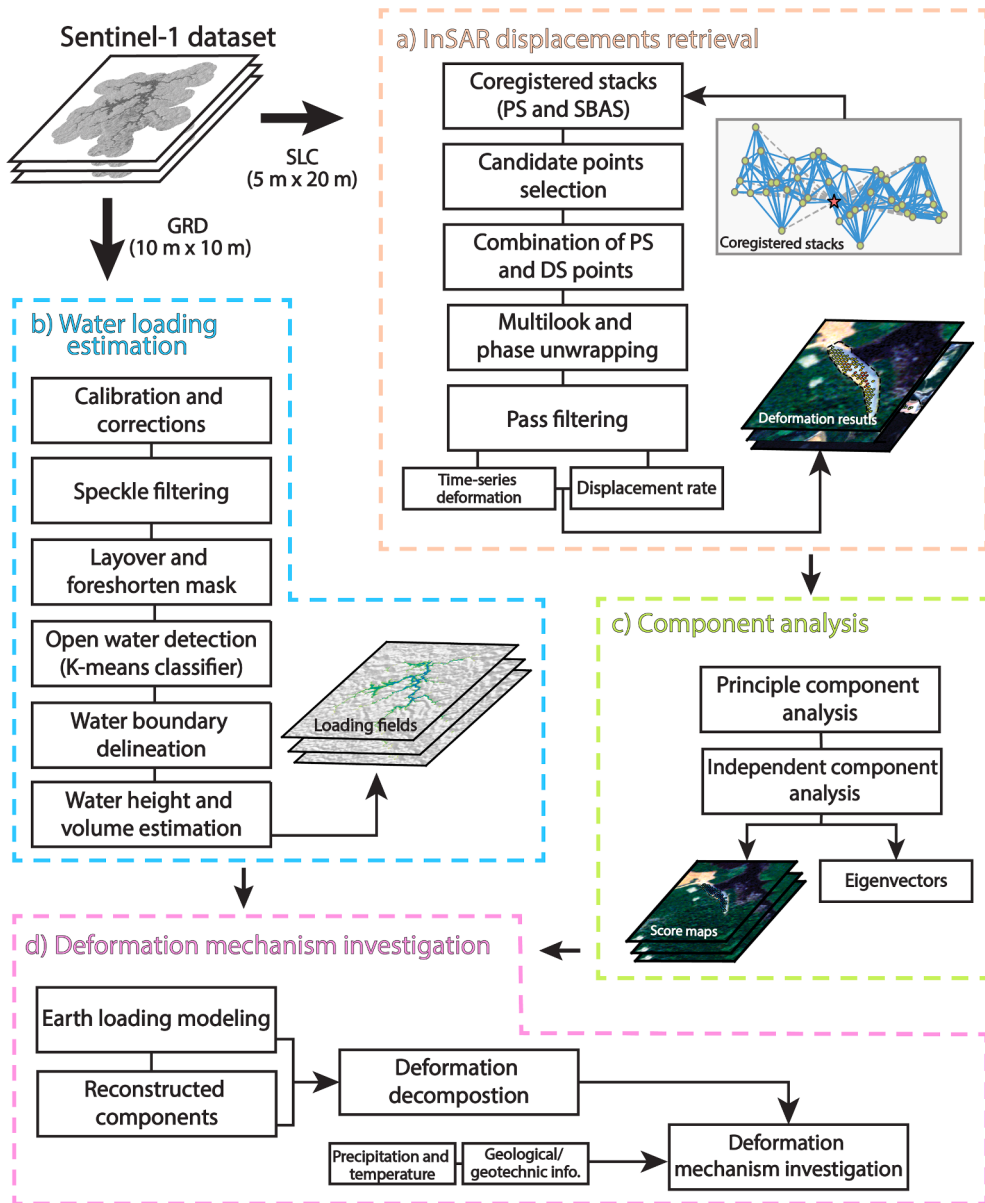


**Fig. 2.** The workflow of data processing and modeling. a) The InSAR displacement retrieval. b) The water loading estimations. c) The signal component analysis. d) The deformation mechanism investigation.

(Latrubesse et al., 2020).

The XPXN project consists of a cluster of dams and other hydraulic facilities (Fig. 1). There are two major rock-fill dams, the Xe Pian (XP) Dam and the Xe Namnoy (XN) Dam, which act as the intakes of the XP and XN Rivers, respectively. These two dams are connected with a ~334-m transfer conduit. In addition, five earth-fill saddle dams were constructed to prevent water from flowing into the natural drainage network (Fig. 1b and Fig. 1e–h). The XPXN reservoir delivers water to the power generators located at the eastern border of the plateau through a 16-km length water-delivery system (Fig. 1j).

On July 23, 2018, Saddle Dam D collapsed after the second phase of water impoundment (Fig. 1a–b and Fig. S1). This dam is a homogeneous earth-fill dam standing above a ~20-m lateritic foundation (Fig. S1b). The dyke has a fold-line-shaped plant with two sections, ~452 m at the northern section and ~322 m at the southern section (Fig. S1b). Both the upstream and downstream slopes are 1:2.5 and are ~30-m height, with an elevation rising to 794 m above sea level (Fig. S1). After the saddle dam failure event, the uncontrolled water flowed southwest into the Xe Pian River and inundated the lower plain, covering an area of ~

36–46 km<sup>2</sup> (Latrubesse et al., 2020). This sudden flood carried mud and debris that hit downstream villages and led to 71 deaths, left thousands homeless, and forced mass resettlement in Attapeu Province (Baird, 2021; Cheng et al., 2019). This flood also had a transboundary impact, which inundated neighboring districts in Stung Treng Province, Cambodia (i.e., ~100 km away from the dam site) (Baird, 2021). The independent expert panel (IEP) concluded that the high permeability of lateritic foundation is the root of the final collapse (Baird, 2021; Schleiss et al., 2019).

### 3. Data and methods

The data-processing and modeling workflow consisted of the following steps (Fig. 2). First, we retrieved dam deformation from InSAR data (Fig. 2a) and estimated the surface loading fields from SAR data (Fig. 2b). Using the InSAR time-series result as the input, we used the component analysis module to obtain independent eigenvectors and score maps (Fig. 2c). The water-loading fields were then fed into the layered Earth loading model. Next, we combined the reconstructed

InSAR results and crustal loading models as a hybrid method to decompose original deformations (Fig. 2d). Finally, we considered meteorological factors (i.e., temperature and precipitation from World Weather Online) and other *in situ* factors (i.e., geological and geotechnical information) to investigate the mechanisms of deformation.

### 3.1. Estimation of water-loading fields

To retrieve water history information from the impoundment (i.e., water level, area, and volume), we identified the open water extent using the amplitude band of SAR images (20170507–20180729, Fig. S2a) and estimated the water volume using a digital elevation model (DEM).

We first preprocessed the Sentinel-1 Ground Range Detected (GRD) product to obtain the radar backscatter ( $\sigma_{DB}^0$ ) using the following four standard steps: (1) precise orbit correction, (2) thermal noise removal, (3) radiometric calibration, and (4) terrain correction. We suppressed the speckle filter in SAR images using a refined Lee filter (Lee et al., 2009). To identify and mask the pixels lying in the foreshortening and layover areas due to the sensor's side-looking geometry, we employed angular-based corrections from volume-scattering and surface-scattering models (Hoekman & Reiche, 2015). We used dual-polarization channels as the inputs of  $k$ -means clustering method for the water segmentation (Arthur & Vassilvitskii, 2006). Here, we set a total 10 clusters based on a random sample of 10,000 pixels to train the classifier. The identified open water extents were converted to water levels by tracing the corresponding pixels of the water boundary and the DEM (Pelich et al., 2021). As the reservoir was initially impounded in 2018, a previously acquired topography model (1 arc-sec SRTM DEM) was applied as the bathymetry to estimate the water-loading fields (Fig. S3).

### 3.2. Retrieval of dam displacement from InSAR

We used 81 Sentinel-1 acquisitions from March 2017 to July 2018 in both descending and ascending orbits to examine the pre-failure surface deformation of the dam. We employed the multi-temporal InSAR technique to separate the possible deformation signals from other nuisance terms in the original interferograms (e.g., atmospheric artifacts and orbital error). Both the Persistent Scatterer (PSInSAR) and Small Baseline Subset (SBAS) techniques were used to characterize the dam deformation owing to their different scattering mechanisms, i.e., persistent or distributed scatterer (Li et al., 2022). Therefore, the InSAR

Scientific Computing Environment (ISCE; Rosen et al., 2012) was used to generate two co-registered interferogram stacks at a full spatial resolution of about  $5 \times 20$  m in the range and azimuth directions, respectively (Fig. S2b–c). In the single-referenced network (i.e., the PS network), the candidate targets are examined by amplitude dispersion and phase stability tests (Hooper, 2008), which maintains most of the long-term coherent targets. To minimize non-correlation and extract the candidate targets that intermittently preserve the coherence, we also used the multi-referenced network (i.e., SBAS) for candidate detection. The phases of candidate targets in both the PS and SBAS networks were then merged using signal-to-noise ratio weights. We resampled the original targets in  $20 \times 20$  m grids to reduce aliasing, and fed these into a semi-3D unwrapping framework. The remaining atmospheric screen were mitigated by a low-pass spatial filter and a high-pass temporal filter. Due to the satellite's polar orbit and oblique side-looking geometry, InSAR measurements are insensitive to horizontal north–south motion. We decomposed the line-of-sight (LOS) deformation into east–west and vertical directions (Fialko et al., 2001) to analyze the dam deformation.

### 3.3. Component analysis of InSAR time-series data

To better understand dam deformation, we used independent component analysis (ICA) to identify and separate the predominant vertical deformation trends. ICA is a class of statistical methods for addressing the blind source separation problem that maximizes non-Gaussianity in mixed sources (e.g., through negentropy) (Ebmeier, 2016).

Based on the ICA method, the mixed signal  $X$  is the product of the source matrix  $S$  (i.e., a set of linear components) and the mixing matrix  $A$  (i.e., the contribution of each independent component), where  $X = AS$ . To assemble the pixel number ( $m$ )  $\times$  epochs ( $n$ ) of the InSAR time-series result, the observation matrix  $X$  are constituted with a set of pixel-wise observations,  $x_i(t)$ . Correspondingly, the mixing matrix  $A$  and source matrix  $S$  are shaped by the number of assumed independent sources,  $ns$ , as follows:

$$\begin{pmatrix} x_1(t) \\ x_2(t) \\ \vdots \\ x_m(t) \end{pmatrix} = \begin{pmatrix} a_1(s) \\ a_2(s) \\ \vdots \\ a_n(s) \end{pmatrix} \cdot \begin{pmatrix} s_1(t) \\ s_2(t) \\ \vdots \\ s_{ns}(t) \end{pmatrix}, \quad (1)$$

To reduce the computational burden, we used a fast fixed-point ICA method (FastICA; Hyvärinen & Oja, 2000). We determined the appropriate number of sources from the principal component analysis (PCA) to avoid the trial-and-error procedure (Chaussard et al., 2017). The rule

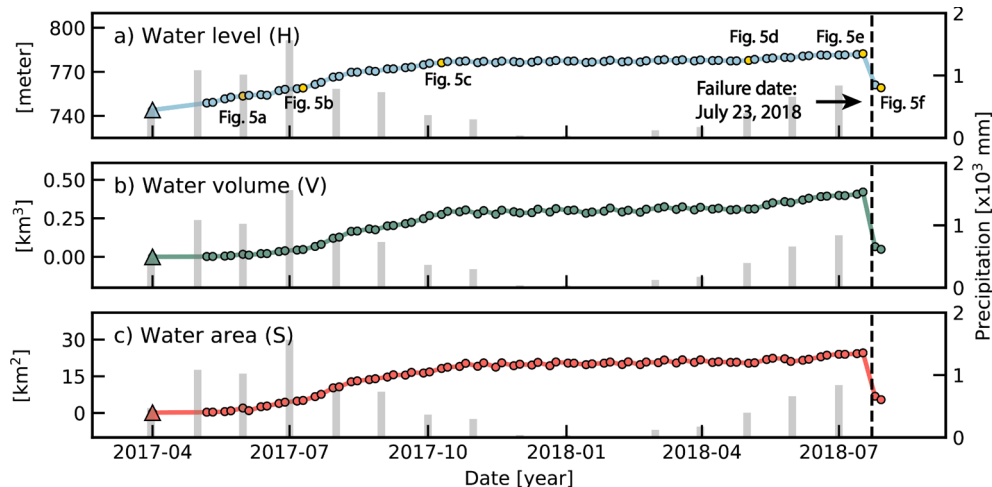


**Fig. 3. Time-series of water variations (April 2017–July 2018).** The triangles represent the reference point. The histograms are the monthly precipitation. The yellow circles in subplot a) denote the representative loading fields in Fig. S4. (For interpretation of the references to color in this figure legend, the reader is referred to the web version of this article.)

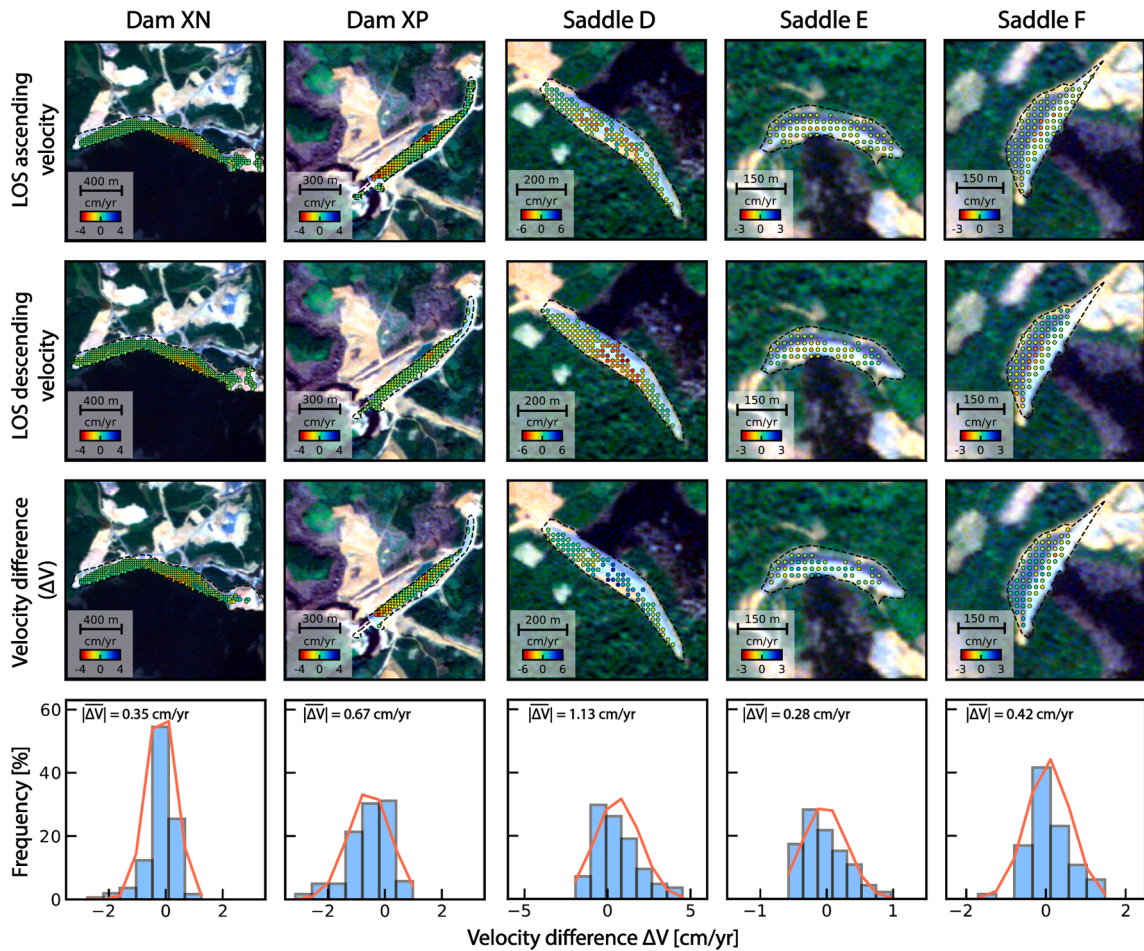


**Fig. 4.** InSAR LOS displacement rates. First row: velocity in ascending track ( $V_{asc}$ ). Second row: velocity in descending track ( $V_{desc}$ ). Third row: the velocity difference ( $\Delta V = V_{asc} - V_{desc}$ ). Fourth row: the histograms of absolute velocity difference ( $|\Delta V|$ ). (Note that different color scales are used for visualization.).

of truncated eigenvalues indicated that the inflection point was located at the fourth principal component (PC), which explained 2% of the dataset (Fig. S4). Retained PCs 1 to 4 above the inflection point contributed to more than 97% of observations. The remaining components most likely reflect high-variability noise (e.g., atmospheric turbulence) rather than solid physical processes. Therefore, we kept the first four informative components and fed these into the ICA framework.

#### 3.4. Modeling surface deformation from water loadings

We modeled the elastic crust deformation from the retrieved surface water loading field to facilitate signal analysis. To simplify the heterogeneous Earth structure, it is common practice to assume that the crust has a spherically symmetric, nonrotating, elastic, and isotropic (SNREI) structure (Farrell, 1972). The elasticity deduced from the Preliminary Reference Earth Model (PREM) was used to generate the load Green's functions (LGFs) (Dziewonski & Anderson, 1981), which represent the spheroidal response towards the unit mass loading (i.e., a 1-kg load) as follows (Farrell, 1972):

$$u_\theta = \frac{A}{m_e} \sum_{n=0}^{\infty} h_n P_n(\cos\theta) \quad (2)$$

$$v_\theta = \frac{A}{m_e} \sum_{n=1}^{\infty} l_n \frac{\partial P_n(\cos\theta)}{\partial \theta},$$

where  $m_e$ ,  $A$ ,  $P_n$ , and  $\theta$  are the Earth's mass, the Earth's radius, Legendre polynomials at the harmonic degree  $n$ , and angular distances between the source load and the target point, respectively; and  $h_n$  and  $l_n$  are the

load Love numbers (LLNs), which represent the horizontal and vertical surface responses, respectively. The LLNs in Eq. 2 were estimated by the asymptotic expression to a harmonic degree of 10,000 to guarantee the estimation accuracy at a localized (km) scale. Finally, we conducted a convolution operation for the LGFs to obtain the combined effect of surface displacement owing to the discrete loadings in the reservoir.

## 4. Results

### 4.1. Water history between 2017 and 2018

Our estimated water history indicated that the reservoir experienced two rounds of impoundment before the collapse in July 2018 (Fig. 3). In the first impoundment cycle (April to October 2017), the water level increased from 744 to 776 m (Fig. 3a). This initial impoundment created a reservoir with a catchment area of  $\sim 18 \text{ km}^2$ , which corresponded to a volumetric gain of  $\sim 0.28 \text{ km}^3$  (Fig. 3c). From November 2017 to April 2018, the reservoir maintained a constant water level of  $777 \pm 0.6 \text{ m}$ . Starting from two months before the dam failure, the second round of impoundment led to a water-level rise of  $\sim 5 \text{ m}$  (from 777 to 782 m). Finally, the collapse of Saddle Dam D released more than 85% of the stored water, equivalent to  $\sim 0.37 \text{ km}^3$  (Fig. S4e-f) and  $> 20 \text{ m}$  water level decreases (Fig. 3a).

### 4.2. InSAR-derived dam deformation

#### 4.2.1. InSAR displacement rates

The retrieved InSAR time-series results from the Sentinel-1 data

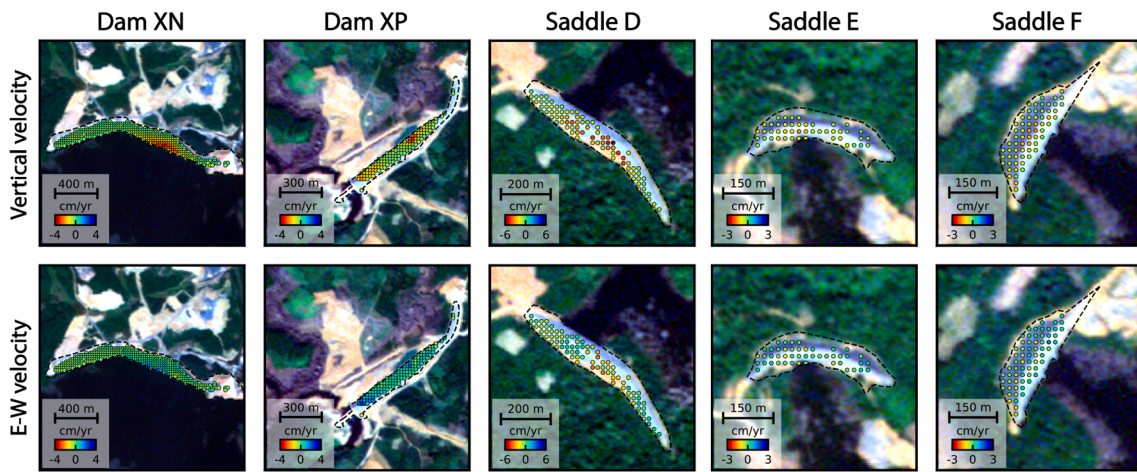


**Fig. 5. The Decomposed vertical and E-W displacement rates.** First row: the displacement rate in the vertical direction; Second row: the displacement rate in the east–west direction. (Note the warm-color represents westward motion).

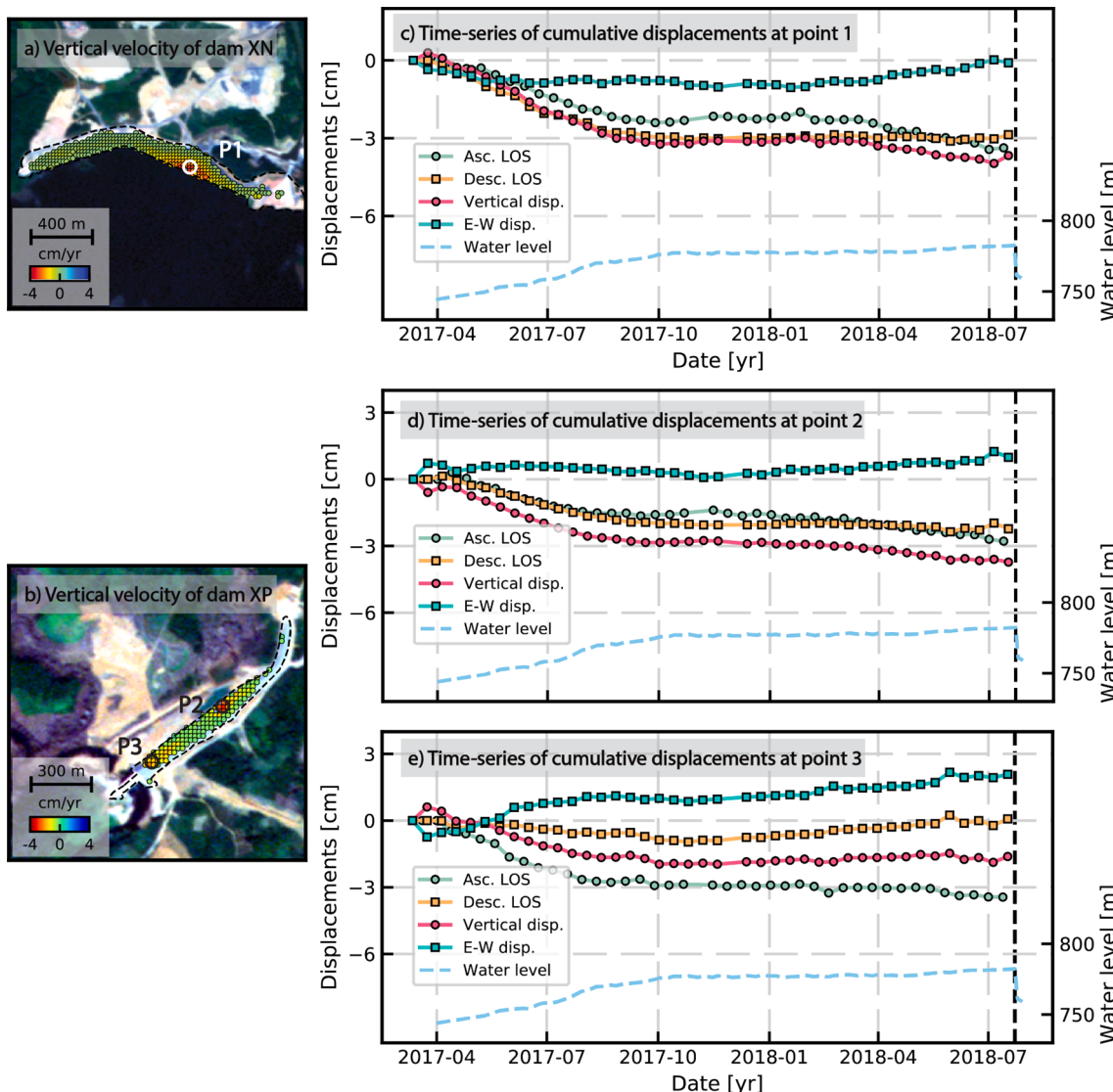


**Fig. 6. The cumulative displacement on two rock-fill dams XN and XP.** a–b) The vertical displacement rates. c–e) The cumulative displacement of selected points, including the LOS displacement and the decomposed vertical and horizontal displacement. The sky-blue lines denote the water level changes. (For interpretation of the references to color in this figure legend, the reader is referred to the web version of this article.)

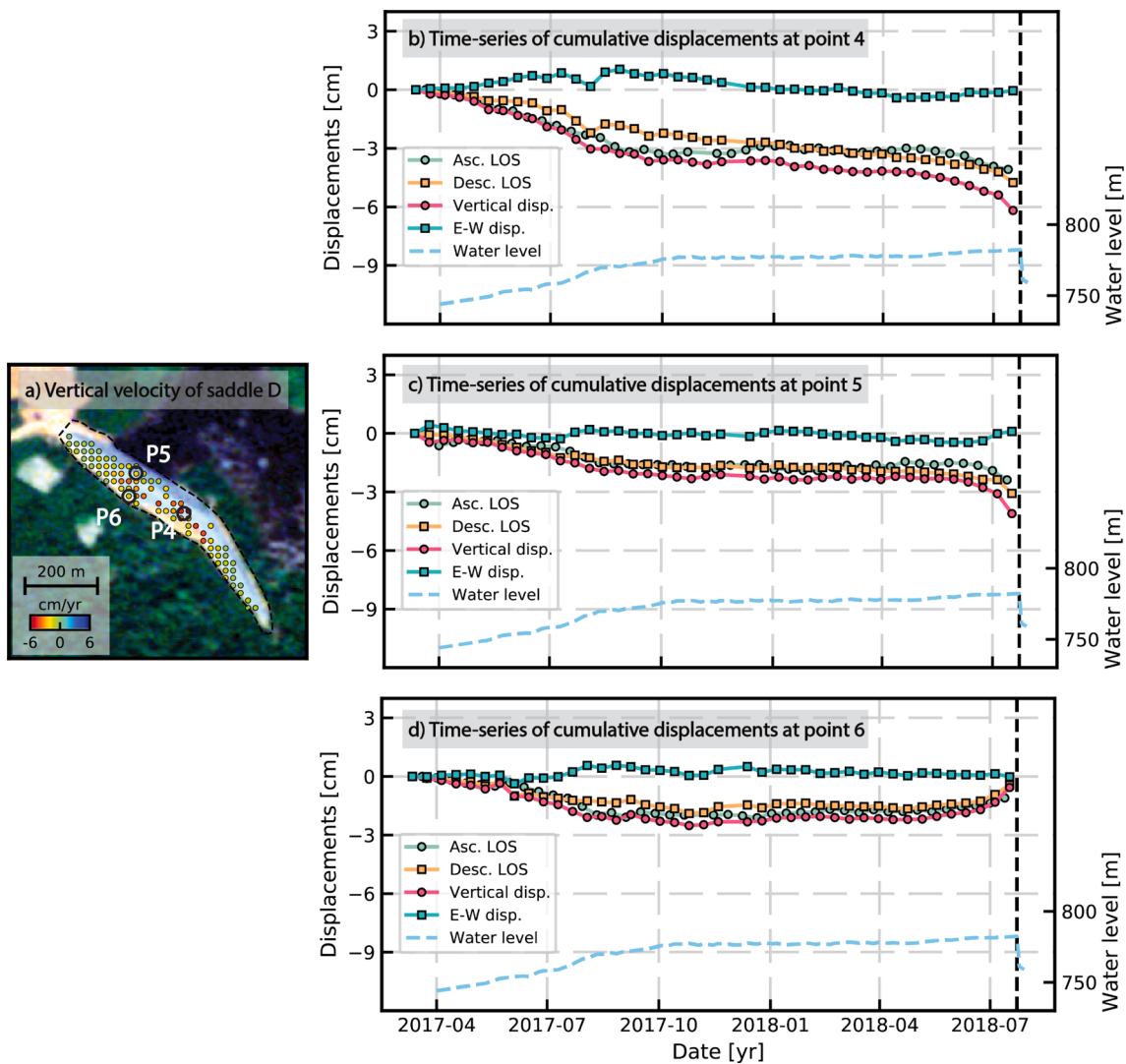


Fig. 7. Similar to Fig. 6, but for earth-fill Saddle Dam D.

revealed pronounced LOS deformation ranging from  $-6$  to  $1$  cm/yr in five out of seven of the XPXN dams (Fig. 4). Saddle dams A and C were not resolvable owing to their small size and changeable surface coverage. The two-track displacement rates agreed well with the velocity divergence  $|\Delta V|$  at  $\sim 0.7$  cm/yr (Fig. 4). This consistent away-motion indicates that the post-construction deformation was predominantly controlled by subsidence. We also found some localized differences in LOS directions (e.g., at the central and western ends of the XP Dam and central section of the Saddle Dam D), which implied potential horizontal deformations.

The decomposed vertical displacement maps further confirm the localized and remarkable degree of subsidence ( $-2$  to  $-6$  cm/yr) during the post-construction period (i.e., April 2017 to July 2018). Most of this localized subsidence ( $>-2$  cm/yr) occurred at the central segments of the dams. Specifically, the subsidence of Saddle Dam D is well constrained in a  $50 \times 350$  m area, reaching a rate of  $-6$  cm/yr. The decomposed east–west displacement rate shows a lower magnitude and narrower spatial distribution than the dominant vertical signal, although the central segment of Saddle Dam D showed a westward motion of up to  $3.6$  cm/yr (Fig. 5).

#### 4.2.2. InSAR time-series displacement

##### 4.2.2.1. Deformation evolution of dams XN and XP. A bowl-shaped

subsidence of the XN Dam (P1 in Fig. 6a) was closely correlated to the reconstructed water-level variations ( $r = 0.89$  in the vertical direction). In the initial impoundment (i.e., April to October 2017), subsidence was up to  $\sim 3$  cm. During the second rainy season, from May to July 2018, an extra  $\sim 0.6$  cm of subsidence was accompanied by a  $\sim 5$ -m rise in the water level. Between the two rounds of impoundment, no significant subsidence occurred ( $<5$  mm/yr). In contrast to the vertical deformation, the horizontal deformation of the XN Dam remained stationary, with almost no cumulative change.

In contrast to the XN Dam, the deformation of the XP Dam decayed logarithmically with time (Fig. 6d–e). In the central and western sections, subsidence from April to October 2017 accounted for 77% (P2) and 81% (P3) of the cumulative subsidence, respectively. Here, the water level variations were less correlated with subsidence ( $r_{p2} = 0.65$  and  $r_{p3} = 0.56$ ). In addition to subsidence, the western section of the XP Dam (near P3) showed an eastward motion of up to  $2$  cm.

**4.2.2.2. Deformation evolution of saddle dams D, E, and F.** The surface deformation of saddle dams D, E, and F also followed a three-period evolution between April 2017 and July 2018. While the first two periods were similar to the XN Dam, the deformation of these three dams was characterized by an acceleration between May and July 2018. During the first impoundment, the central crest (P4), upstream slope (P5), and the downstream slope (P6) were subsiding at rates from  $-3.7$

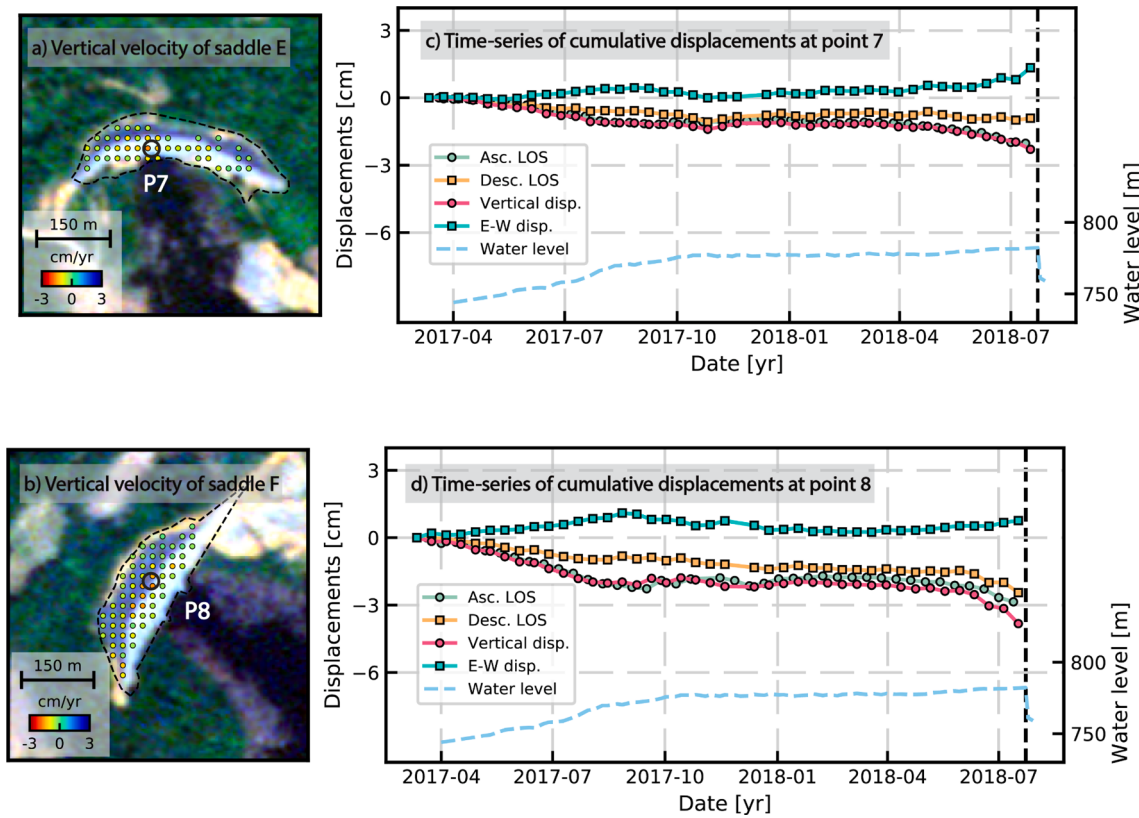


**Fig. 8.** Similar to Fig. 6, but for saddle dams E and F.

to  $-5.8 \text{ cm/yr}$  (Fig. 7b-d). Two months before its failure, the surface deformation accelerated twice, reaching up to  $\sim 13 \text{ cm/yr}$ . Interestingly, while the upstream and crest areas showed a greater sinking rate, the downstream slope was uplifted by 2 cm during this period (Fig. 7d). Similar to the collapsed Saddle Dam D, we also observed a “subsiding-stagnant-accelerating” pattern for the other two saddle dams. Compared to Saddle Dam D, saddle dams E and F experienced a lower rate of deformation during the initial impoundment period ( $<-3 \text{ cm/yr}$ ) and the acceleration period ( $<-9 \text{ cm/yr}$ ) (Fig. 8). This similar accelerating subsidence on the saddle dams E and F indicates the potential risks of dam-break in the future.

#### 4.3. Decomposition of the Saddle dam D deformation signals

##### 4.3.1. Independent components from the ICA

The ICA successfully decomposed vertical deformation into four distinct patterns based on eigenvector time series, i.e., piecewise decreasing, a time-decaying trend, seasonal variations, and abrupt changes (Fig. 9). The first independent component (IC-1) accounted for the dominant deformation, which contributed to 70% of the eigenvalues. This represents the large and extensive subsidence signals across Saddle Dam D after construction (Fig. 9a). The time series of IC-1 eigenvectors highlight the two periods of subsidence from April to October 2017 and May to July 2018. The temporal pattern of the eigenvector agrees well with the water-level changes in the reservoir ( $r = 0.87$ ). Spatially, the corresponding score map suggests that the dam surface was most responsive at the center of the dam body (Fig. 9e).

Similar to IC-1, the spatial distribution of the second component (IC-2) was also widespread across the dam body (Fig. 9f). This showed a continuous subsiding feature irrespective of reservoir impoundment. More than 85% of the downward motion was completed in 2017. This logarithmic pattern of the IC-2 eigenvector is more likely indicative of compaction under the weight of the dam body (Fig. 9b).

The third component, IC-3, captured the seasonal variation of

deformation throughout the observation period; a negative trend was observed between May and October 2017 and a positive slope from November 2017 to May 2018 (Fig. 9c). By examining the temperature record near the reservoir, we also found that this pattern was highly correlated with variations in temperature ( $r = 0.88$ ).

The fourth component, IC-4, showed an abrupt change two months before the dam failure (Fig. 9d). The heterogeneous score distribution on the downstream slope indicates an opposite surface response before the dam failure (Fig. 9h). The spatial pattern of the score map was consistent with our observations for Saddle Dam D, for which the direction of deformation in the downstream slope was reversed to the crest and upstream slope.

##### 4.3.2. Reconstructed deformations from the ICA

The deformation reconstructions show that the original signals are well represented by the retrieved signals (average RMS  $< 1 \text{ mm}$ ; Fig. 10a). The vertical displacement from IC-1 contributes  $\sim 1.7 \text{ cm}$  and exhibits a homogenous spatial distribution dam (Fig. 10b). The deformation associated with IC-2 reaches up to 2.6 cm on the crest but only 1 cm in the slope areas (Fig. 10c). The seasonal variations associated with IC-3 show low amplitudes ( $\sim 0.4 \text{ cm}$ ) and similar annual phases (Fig. 10d). The reconstructed IC-4 represents sudden changes before dam failure, with a stable tendency before May 2018. The uplift of the downstream slope accounts for deformation of 2.1 cm, while the crest and upstream show movements in the opposite direction of 2 cm and 1.7 cm, respectively (Fig. 10e).

##### 4.3.3. Deformation of Saddle dam D induced by water loading

According to the layered Earth loading model, the vertical deformation induced by water masses ranged from 0.95 cm to 1.25 cm (Fig. 11a). The increasing subsidence rates from the south to north section indicate the spatial heterogeneity of the mass distribution. At points P4-P6, the degree of loading displacement accounted for 55%–63% of IC-1 (Fig. 11b-d). The residuals of IC-1 and the loading model

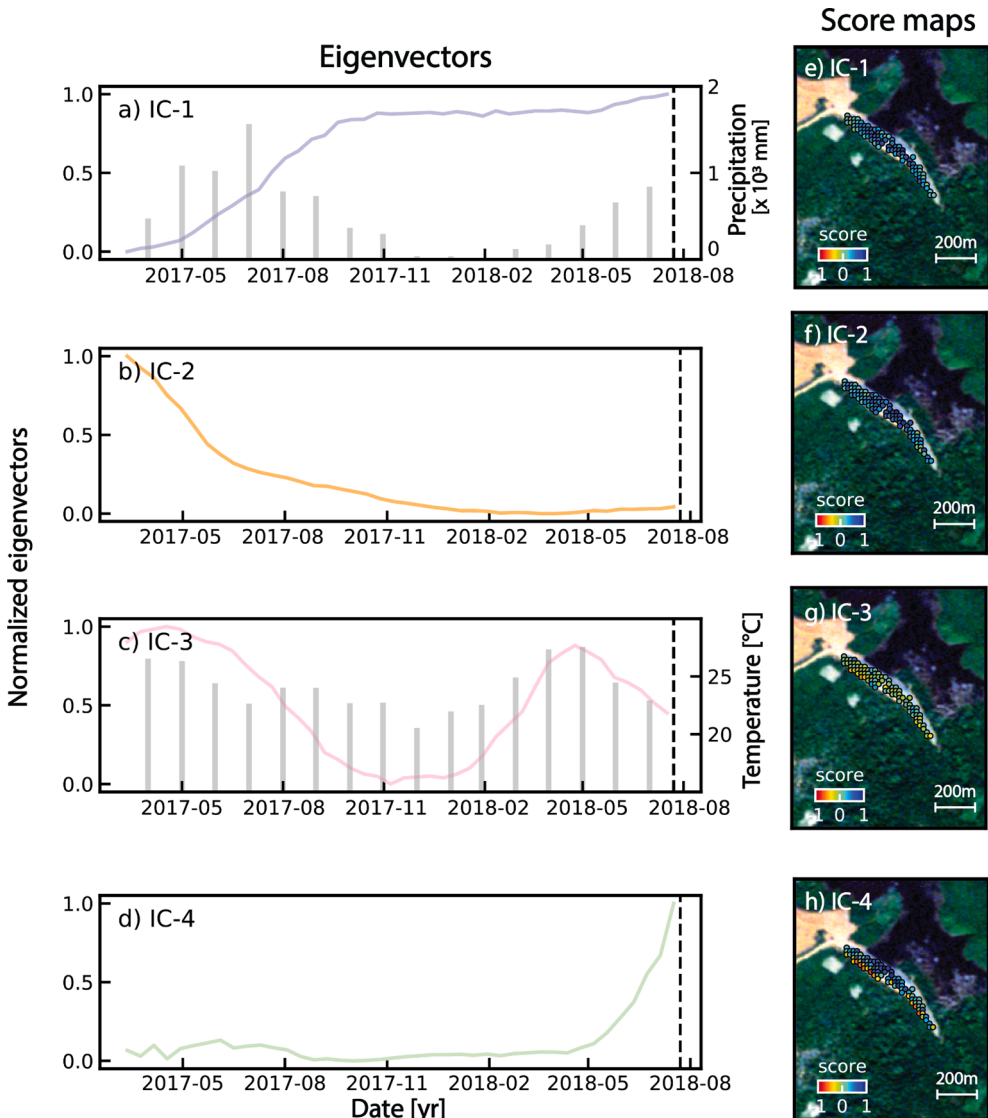


**Fig. 9.** The independent component analysis for vertical displacements on Saddle Dam D. a-d) The time-series of eigenvectors of components IC 1–4. The histograms of precipitation and rainfall were depicted in the background. e-h) The normalized independent component scores on the Saddle Dam D.

predictions are higher for the upstream slope, reaching 0.8 cm before the dam failure (Fig. 11d).

## 5. Discussion

### 5.1. Deformation mechanism of Saddle dam D

The retrieved independent components indicate that there were at least four different physical processes behind the Saddle Dam D. The correlation analysis explicitly indicates that the vertical displacements for IC-1 and IC-3 are linked to changes in the water volume and thermal effects, respectively (Fig. 12). The other two components are the time-decaying process of IC-2 and the sudden change of IC-4. Considering the statistical model of hydraulic deformation (Shao et al., 2018; Yuan et al., 2020), the deformation evolution of Saddle Dam D can be expressed as follows:

$$\delta = \delta_W + \delta_T + \delta_\theta + \delta_A \quad (4)$$

where  $\delta_W$  is the water pressure component,  $\delta_T$  is the temperature component,  $\delta_\theta$  is the time-decaying component, and  $\delta_A$  is the precursory acceleration component.

The water-pressure-associated deformation component  $\delta_W$  can be characterized as follows. First, hydrostatic pressure exerts a perpendicular force on the upstream slope, which results in subsidence of the dam surface, i.e.,  $\delta_{W1}$  (Fig. 12a). Second, the effect of gravity on the water mass transforms the shapes of the bedrock and the foundation beneath the dam body, i.e.,  $\delta_{W2}$  (Fig. 12b). However, the decomposition component IC-1 failed to identify  $\delta_{W1}$  and  $\delta_{W2}$  (Fig. 11a). Mathematically, this is not unexpected as  $\delta_{W1}$  and  $\delta_{W2}$  are statistically dependent in the temporal domain (Chaussard & Farr, 2019). Therefore, our prior assumption of converting the original signal into maximum independent components by retrieving the base functions cannot be adapted for  $\delta_W$  (Ebmeier, 2016). The time-decaying subsidence rate associated with IC2 suggests a consolidation process due to soil grain rearrangement (Fig. 12c; Terzaghi et al., 1996). The amplitude of the consolidation component ( $\sim 2.6$  cm vs. 1 cm) is relevant to the height of the dam (Fig. 10c), whereby the drainage and creep effects are more notable for higher portions of dams owing to the stacking volume of the soil. The seasonal temperature variation explained the third component of deformation, denoting a thermal dilation effect of soil particles (Fig. 10d and Fig. 12d; Scaioni et al., 2018). However, the homogenous thermal response is not agree with the thermal-related deformation observed for other concrete dams (Wang et al., 2011). This may reflect the lower

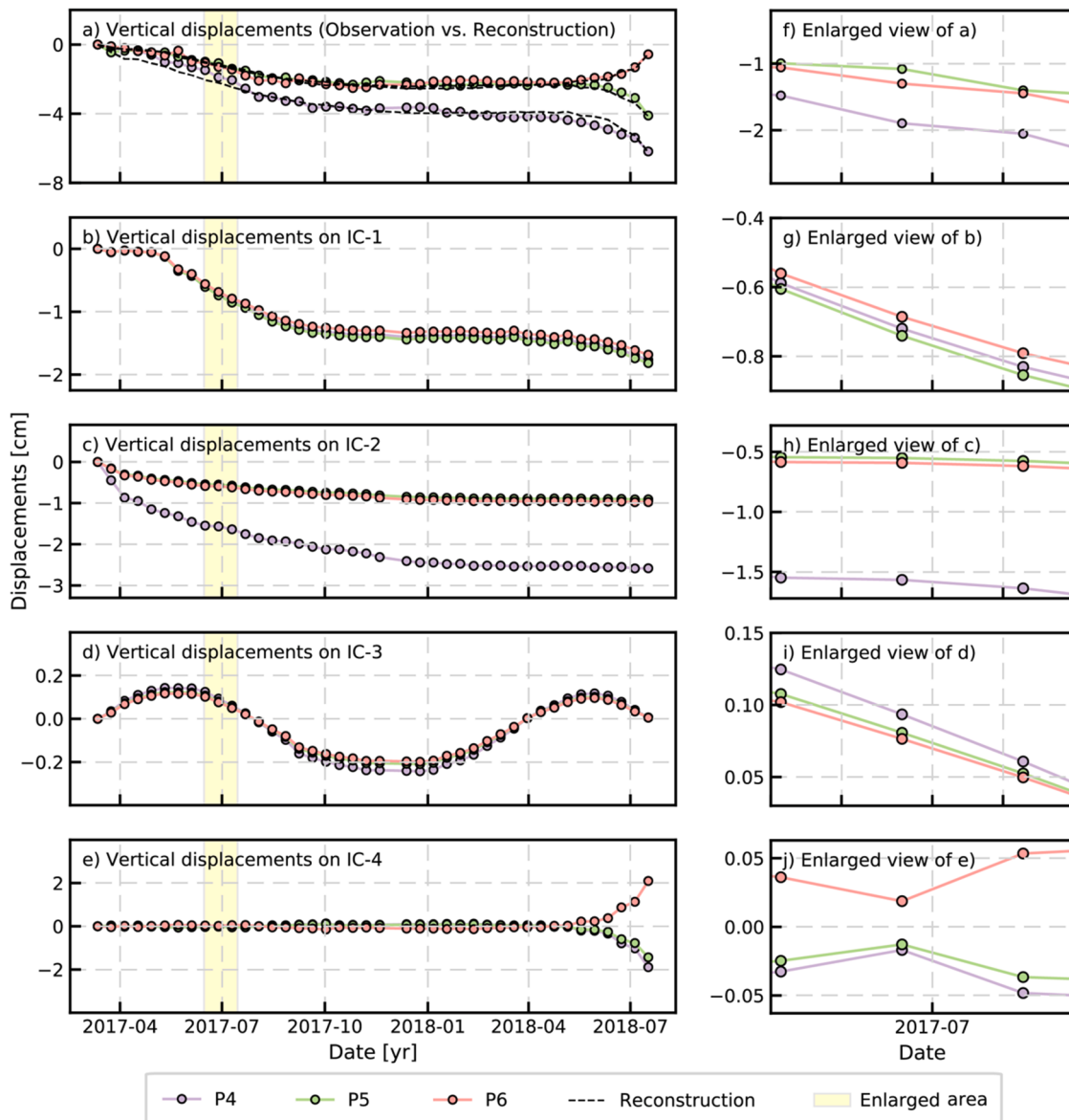


**Fig. 10.** The reconstructed deformation on Saddle Dam D. a) The observed and the reconstructed deformations. b)–e) The time-series of the dam deformation for the IC 1–4. f)–j) The corresponding enlarged views of a)–e).

coefficient of thermal expansion (CTE) for the filled earth dams (e.g., sandstone CTE =  $9.6 \times 10^{-6}/^{\circ}\text{C}$  and basalt CTE =  $7.8 \times 10^{-6}/^{\circ}\text{C}$ ; (Hein & Sullivan, 2012)) compared to concrete (e.g., saturated cement CTE =  $18\text{--}20 \times 10^{-6}/^{\circ}\text{C}$ ; (Chung & Shin, 2011)). In addition, the combined influences of other dominant deformation sources (i.e., water pressure and consolidation) may superimpose the thermal effect.

The accelerating subsidence on the upstream slope and crest of Saddle Dam D reveals that the upstream slope could not support the increasing water pressure before its collapse. According to the IEP report, the deterioration in upstream slope stability was triggered by uncontrolled seepage and erosion of the heterogeneous foundation and dam body (Schleiss et al., 2019). The internal drainage system was unable to constrain the phreatic line within the dam. Therefore, with further impoundment from June 2018, uncontrolled seepage passed through the dam body, and the highest part of the dam could not withstand the additional mass. The continuous and accelerating subsidence acting on the upstream and crest sections led to a sliding mass moving in a downstream direction, which finally resulted in uplift motion at the downstream slope (Fig. 12e). In addition, the InSAR data

show an undulating area at the downstream slope consistent with the *in situ* observations approximately  $\sim 10$  h before the dam failure (10:35 a.m. local time on July 23, 2018; Schleiss et al., 2019). Considering both the *in situ* evidence and satellite observations, we suggest that the acceleration in deformation before the dam failure was caused by seepage and erosion in the dam body, with the continuous sinking of the upper portion leading to lateral extrusion downstream.

## 5.2. Wider implications

We highlight several recommendations for the remaining XPXN project dams from our observation and analysis. Although there was no anomalous signal for these two rock-fill XP and XN dams, the vulnerability delineation (i.e., areas outside the 25th and 75th percentiles; Fig. 13a–b) identifies differential deformation, which reflects loosened or softened zones in their dam body (Talukdar & Dey, 2021). These differential deformations may promote transverse and longitudinal cracks, leading to progressive hazards in future. Moreover, the remaining saddle dams E and F are noteworthy because they exhibit a

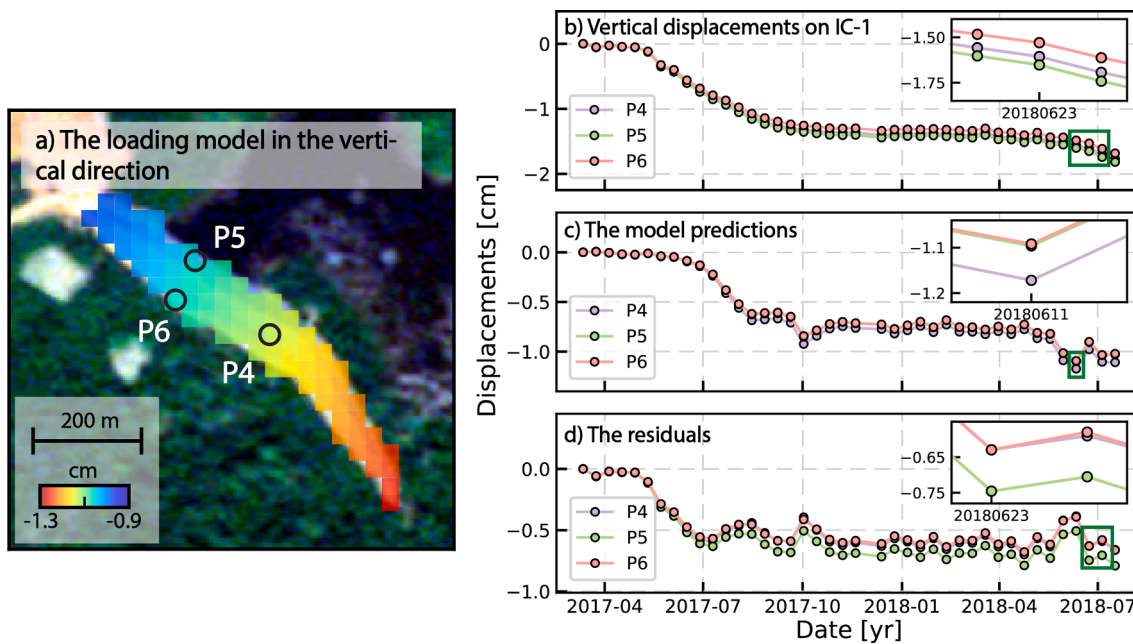


**Fig. 11.** The decomposition result of IC-1 components. a) The model predictions in the vertical direction. b) The original IC-1 component. c) The model predictions. d) The residual between the IC-1 and model predictions. The green rectangles denote the extents of enlarged views. (For interpretation of the references to color in this figure legend, the reader is referred to the web version of this article.)

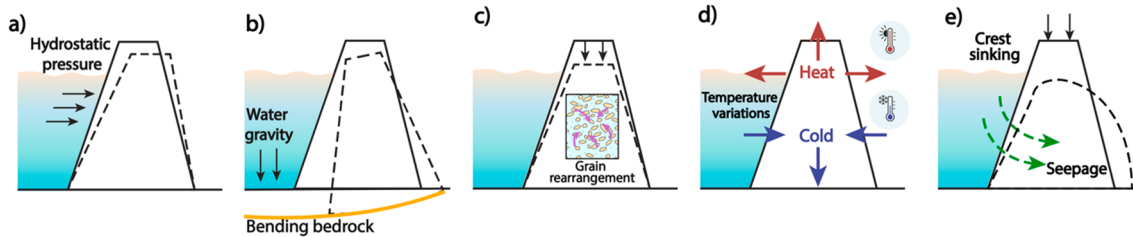


**Fig. 12.** The schematic sketch for the deformation on the Saddle Dam D. a) hydrostatic pressure; b) water gravity; c) soil consolidation; d) temperature effect; e) continuous crest sinking and lateral extrusion.

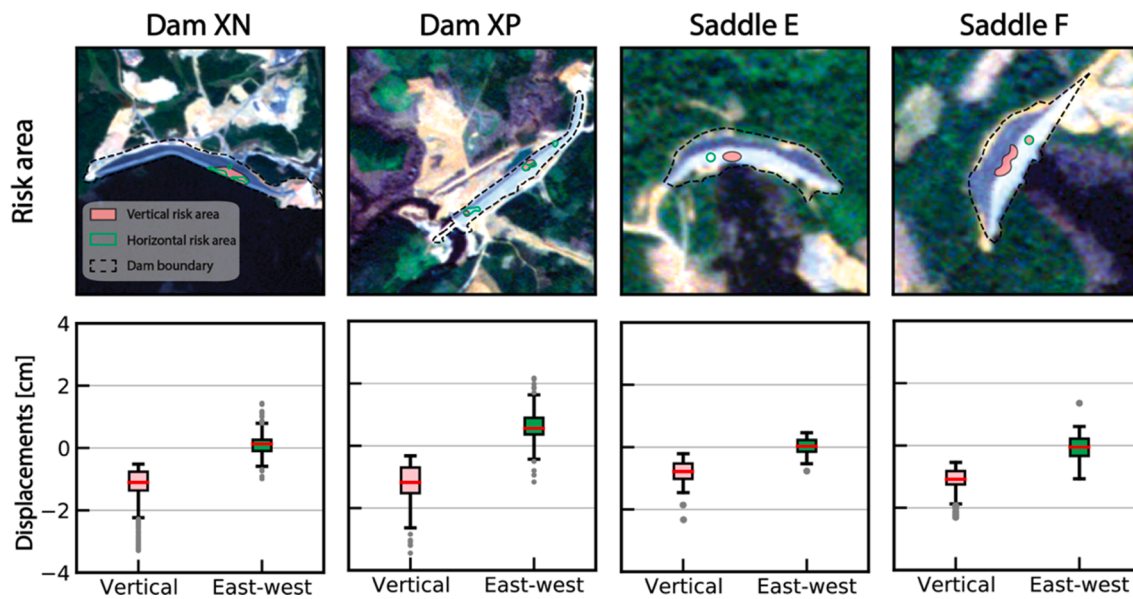


**Fig. 13.** The risk areas on the standing dams from displacement rates. First row: the area of horizontal indicated risk area and vertical indicated risk area. Second row: boxplots of vertical and horizontal displacement rates (the red lines denote the mean values). (For interpretation of the references to color in this figure legend, the reader is referred to the web version of this article.)

similar accelerating deformation pattern as the collapsed Saddle Dam D; the central sections of these two dams show a risk area of ~1,200 and ~3,000 m<sup>2</sup>, respectively (Fig. 13c–f). The post-failure site investigation also documented that the uncontrolled resurgence and the seeping zone were close to the downstream area of Saddle Dam E (Schleiss et al., 2019), indicating the existing internal erosion and softening. Furthermore, because the heterogeneous lateritic foundation is the residual soil, this may allow the movement of water through the foundation, which further increases sensitivity to uncontrolled time-dependent settlement. Considering the comparable design and deformation pattern (e.g., filling materials and foundation), substantial seepage control treatments are recommended to prevent possible water leakage.

While comprehensive dam monitoring cannot be achieved by any standalone technique, radar satellites provide a quantitative basis for detecting abnormal dam motion and identifying risk areas. Indeed, the affordable, broad spatial coverage, and weather-independent characteristics of radar satellites make them a useful tool for dam-surface monitoring. In particular, our results attest to the applicability of this technique to small-to-medium-sized dams in humid and vegetated areas. As set out by the Laos government, a 10,000-MW hydropower capacity increase will be established in the next decade to support economic development both domestically and internationally, with more than 50 sites currently under construction (Baird, 2021). With such a considerable increase in dams alongside currently limited *in situ* monitoring, we strongly advocate establishing a radar satellite-based surveillance system through collaborative efforts between regulators, academics, and energy companies to support hydropower energy development.

## 6. Conclusions

We investigate the spatial and temporal variability of dam motion and reservoir operations in the XPXN project, Laos, using SAR data, ICA method, and a numerical loading model. We find that water pressure, soil consolidation, thermal expansion, and sink and lateral extrusion were the major mechanisms driving the deformation and collapse of Saddle Dam D. Based on our results, we draw the following conclusions:

- 1) The rock-fill XP and XN Dams were relatively stable after the first initial impoundment. However, the central part of the eastern section of the XN Dam, and the central crest of the XP Dam, are vulnerable areas with cm-scale subsidence. The western section of the XP Dam shows continuous eastern motion at a rate of ~1.5 cm/yr, suggesting that a differential deformation area needs to be monitored.
- 2) The Saddle Dam D showed an abnormal sinking with maximum of 13 cm/yr two month before the final collapse. Other earth-fill saddle dams E and F showed similar accelerating subsidence rates exceeding 9 cm/yr. Special attention should be paid to assessing whether further undesirable deformation will occur in Saddle Dams E and F. We suggest that seepage control and slope reinforcement interventions are critical for these saddle dams, otherwise, future dam-break events will be highly possible. The dam authority and surveillance team should be able to know the degradation and issue the hazard warning to downstream areas in a timely manner (Baird, 2021), if more careful and routine surveillance can be arranged.
- 3) The current strategy of seasonal impoundment and release at the XPXN project should avoid rapid seasonal variations in water levels, and the maximum water storage capacity in the reservoir should be reduced. In addition, the precursory deformation and underpinning mechanisms in collapsed Saddle Dam D provide an important early warning baseline for future operations.

Overall, our investigation of the XPXN hydropower project and the Saddle Dam D failure shed new insights into hazard assessment and monitoring of small-to-medium-sized dams. The study reveals the detailed evolution of dam deformation before the failure event, and indicates the ongoing risk for the remaining dams in XPXN project.

Lessons learnt from XPXN further emphasize the importance of dam monitoring and catastrophic consequences caused by negligence and poor management from the dam authority. With the growing demand for hydropower development in densely populated and developing countries, space-borne monitoring offers a useful tool for evaluating potential risks throughout the lifecycle of dam operations.

## CRediT authorship contribution statement

**Lei Xie:** Writing – original draft, Conceptualization, Methodology, Investigation, Visualization. **Wenbin Xu:** Conceptualization, Investigation, Formal analysis, Writing – review & editing, Supervision. **Xiaoli Ding:** Formal analysis, Writing – review & editing, Supervision.

## Declaration of Competing Interest

The authors declare that they have no known competing financial interests or personal relationships that could have appeared to influence the work reported in this paper.

## Acknowledgements

The research is supported by the National Natural Science Foundation of China under Grant (42174023). It is also supported by the Research Grants Council of the Hong Kong Special Administrative Region (PolyU 152232/17E, PolyU 152164/18E558, and PolyU 152233/19E). Sentinel-1 SLC and GRD data are acquired from the Alaska Satellite Facility (<https://www.asf.alaska.edu/>), and Google Earth Engine (<https://developers.google.com/earth-engine/datasets>), respectively. The RapidEye-3 image is from Planet research/education program (<https://www.planet.com/markets/education-and-research/>). The meteorological data are from World Weather Online (<https://www.worldweatheronline.com>). Some figures were prepared by the Generic Mapping Tools 6.0 (<http://gmt.soest.hawaii.edu/home>).

## Appendix A. Supplementary material

Supplementary data to this article can be found online at <https://doi.org/10.1016/j.jag.2022.102797>.

## References

- Arthur, D., Vassilvitskii, S., 2006. k-means++: The advantages of careful seeding. Stanford.
- Baird, I.G., 2021. Catastrophic and slow violence: Thinking about the impacts of the Xe Pian Xe Namnoy dam in southern Laos. J. Peasant Studies 48 (6), 1167–1186. <https://doi.org/10.1080/03066150.2020.1824181>.
- Chaussard, E., Farr, T.G., 2019. A new method for isolating elastic from inelastic deformation in aquifer systems: Application to the San Joaquin Valley, CA. Geophys. Res. Lett. 46 (19), 10800–10809. <https://doi.org/10.1029/2019GL084418>.
- Chaussard, E., Milillo, P., Bürgmann, R., Perissin, D., Fielding, E.J., Baker, B., 2017. Remote sensing of ground deformation for monitoring groundwater management practices: Application to the Santa Clara Valley during the 2012–2015 California drought. J. Geophys. Res. Solid Earth 122 (10), 8566–8582. <https://doi.org/10.1002/2017JB014676>.
- Cheng, S., Zhao, W., Yin, Z., 2019. PS-InSAR analysis of collapsed dam and extraction of flood inundation areas in Laos using Sentinel-1 SAR images. In: 2019 IEEE 4th Advanced Information Technology, Electronic and Automation Control Conference (IAEAC), pp. 2605–2608. <https://doi.org/10.1109/IAEAC47372.2019.8997848>.
- Chung, Y., Shin, H.-C., 2011. Characterization of the coefficient of thermal expansion and its effect on the performance of Portland cement concrete pavements. Can. J. Civ. Eng. 38 (2), 175–183. <https://doi.org/10.1139/L10-122>.
- Dziewonski, A.M., Anderson, D.L., 1981. Preliminary reference Earth model. Phys. Earth Planet. Inter. 25 (4), 297–356. [https://doi.org/10.1016/0031-9201\(81\)90046-7](https://doi.org/10.1016/0031-9201(81)90046-7).
- Ebmeier, S.K., 2016. Application of independent component analysis to multitemporal InSAR data with volcanic case studies: ICA Analysis of InSAR Data. J. Geophys. Res. Solid Earth 121 (12), 8970–8986. <https://doi.org/10.1002/2016JB013765>.
- Farrell, W.E., 1972. Deformation of the Earth by surface loads. Rev. Geophys. 10 (3), 761. <https://doi.org/10.1029/RG010i003p00761>.
- Fialko, Y., Simons, M., Agnew, D., 2001. The complete (3-D) surface displacement field in the epicentral area of the 1999 MW 7.1 Hector Mine Earthquake, California, from space geodetic observations. Geophys. Res. Lett. 28 (16), 3063–3066. <https://doi.org/10.1029/2001GL013174>.

- Hein, D. K., Sullivan, S., 2012. Concrete coefficient of thermal expansion (CTE) and its significance in mechanistic-empirical pavement design. In: Proceedings, Annual Conference of Canada, Fredericton, New Brunswick.
- Hoekman, D.H., Reiche, J., 2015. Multi-model radiometric slope correction of SAR images of complex terrain using a two-stage semi-empirical approach. *Remote Sens. Environ.* 156, 1–10. <https://doi.org/10.1016/j.rse.2014.08.037>.
- Hooper, A., 2008. A multi-temporal InSAR method incorporating both persistent scatterer and small baseline approaches. *Geophys. Res. Lett.* 35 (16), L16302. <https://doi.org/10.1029/2008GL034654>.
- Hyyvärinen, A., Oja, E., 2000. Independent component analysis: Algorithms and applications. *Neural Netw.* 13 (4–5), 411–430. [https://doi.org/10.1016/S0893-6080\(00\)00026-5](https://doi.org/10.1016/S0893-6080(00)00026-5).
- Latrubbles, E.M., Park, E., Sieh, K., Dang, T., Lin, Y.N., Yun, S.-H., 2020. Dam failure and a catastrophic flood in the Mekong basin (Bolaven Plateau), southern Laos, 2018. *Geomorphology* 362, 107221. <https://doi.org/10.1016/j.geomorph.2020.107221>.
- Lee, J.-S., Wen, J.-H., Ainsworth, T.L., Chen, K.-S., 2009. Improved sigma filter for speckle filtering of SAR imagery. *IEEE Trans. Geosci. Remote Sens.* 47 (1), 202–213. <https://doi.org/10.1109/TGRS.2008.2002881>.
- Lempérière, F., 2017. Dams and floods. *Engineering* 3 (1), 144–149. <https://doi.org/10.1016/J.ENG.2017.01.018>.
- Li, X., Li, Y., Lu, X., Wang, Y., Zhang, H., Zhang, P., 2020. An online anomaly recognition and early warning model for dam safety monitoring data. *Struct. Health Monitoring* 19 (3), 796–809. <https://doi.org/10.1177/1475921719864265>.
- Li, S., Xu, W., Li, Z., 2022. Review of the SBAS InSAR time-series algorithms, applications and challenges. *Geod. Geodyn.* 13 (2), 114–126. <https://doi.org/10.1016/j.geog.2021.09.007>.
- Milillo, P., Perissin, D., Salzer, J.T., Lundgren, P., Lacava, G., Milillo, G., Serio, C., 2016. Monitoring dam structural health from space: Insights from novel InSAR techniques and multi-parametric modeling applied to the Pertusillo dam Basilicata, Italy. *Int. J. Appl. Earth Obs. Geoinf.* 52, 221–229. <https://doi.org/10.1016/j.jag.2016.06.013>.
- Moran, E.F., Lopez, M.C., Moore, N., Müller, N., Hyndman, D.W., 2018. Sustainable hydropower in the 21st century. *Proc. Natl. Acad. Sci.* 115 (47), 11891–11898. <https://doi.org/10.1073/pnas.1809426115>.
- Pelich, R., Chini, M., Hostache, R., Matgen, P., Pulvirenti, L., Pierdicca, N., 2015. Mapping floods in urban areas from dual-polarization InSAR coherence data. *IEEE Geosci. Remote Sens. Lett.* 1–5. <https://doi.org/10.1109/LGRS.2021.3110132>.
- Pisaniello, J.D., Dam, T.T., Tingey-Holyoak, J.L., 2015. International small dam safety assurance policy benchmarks to avoid dam failure flood disasters in developing countries. *J. Hydrol.* 531, 1141–1153. <https://doi.org/10.1016/j.jhydrol.2015.09.077>.
- Roque, D., Lima, J.N., Perissin, D., Falcão, A.P., Lemos, J.V., Fonseca, A.M., 2021. Integrated InSAR and GNSS monitoring subsystem for an arch dam and reservoir banks. *J. Surv. Eng.* 147 (3), 05021003. [https://doi.org/10.1061/\(ASCE\)SU.1943-5428.0000361](https://doi.org/10.1061/(ASCE)SU.1943-5428.0000361).
- Rosen, P.A., Gurrola, E., Sacco, G.F., Zebker, H., 2012, April 23. The InSAR scientific computing environment. 9th European Conference on Synthetic Aperture Radar, Nuremberg, Germany.
- Sanematsu, K., Moriyama, T., Sotouky, L., Watanabe, Y., 2011. Mobility of rare Earth elements in basalt-derived laterite at the Bolaven Plateau, southern Laos: Mobility of rare earth elements in laterite. *Resour. Geol.* 61 (2), 140–158. <https://doi.org/10.1111/j.1751-3928.2011.00155.x>.
- Sciaioni, M., Marsella, M., Crosetto, M., Tornatore, V., Wang, J., 2018. Geodetic and remote-sensing sensors for dam deformation monitoring. *Sensors* 18 (11), 3682. <https://doi.org/10.3390/s18113682>.
- Schleiss, A.J., Tournier, J.-P., Chraibi, A.F., 2019. Report of Independent Expert Panel (IEP) Xe-Pian Xe-Namnoy project failure of Saddle Dam D.
- Shao, C., Gu, C., Yang, M., Xu, Y., Su, H., 2018. A novel model of dam displacement based on panel data. *Struct. Control Health Monitoring* 25 (1), e2037. <https://doi.org/10.1002/stc.2037>.
- Talukdar, P., Dey, A., 2021. Finite element analysis for identifying locations of cracking and hydraulic fracturing in homogeneous earthen dams. *Int. J. Geo-Eng.* 12 (1), 10. <https://doi.org/10.1186/s40703-020-00139-8>.
- Terzaghi, K., Peck, R.B., Mesri, G., 1996. *Soil mechanics in engineering practice*, (3rd ed.). Wiley.
- Wang, T., Perissin, D., Rocca, F., Liao, M.-S., 2011. Three Gorges Dam stability monitoring with time-series InSAR image analysis. *Sci. China Earth Sci.* 54 (5), 720–732. <https://doi.org/10.1007/s11430-010-4101-1>.
- Yuan, D., Wei, B., Xie, B., Zhong, Z., 2020. Modified dam deformation monitoring model considering periodic component contained in residual sequence. *Struct. Control Health Monitoring* 27 (12), e2633. <https://doi.org/10.1002/stc.2633>.